

1 **Enhanced 20th century heat transfer to the Arctic simulated**
2 **in the context of climate variations over the last millennium**

3
4 **J.H. Jungclaus, K. Lohmann, and D. Zanchettin**

5
6 {Max Planck Institut für Meteorologie, Hamburg, Germany}

7
8 Correspondence to: J. H. Jungclaus (johann.jungclaus@mpimet.mpg.de)

9
10 **Abstract**

11 Oceanic heat transport variations, carried by the northward flowing Atlantic Water, strongly
12 influence Arctic sea-ice distribution, ocean-atmosphere exchanges, and pan-Arctic temperatures.
13 Paleoceanographic reconstructions from marine sediments near Fram Strait have documented a
14 dramatic increase in Atlantic Water temperatures over the 20th century, unprecedented in the last
15 millennium. Here we present results from Earth system model simulations that reproduce and
16 explain the reconstructed exceptional Atlantic Water warming in Fram Strait in the 20th century in
17 the context of natural variability during the last millennium. The associated increase in ocean heat
18 transfer to the Arctic can be traced back to changes in the ocean circulation in the sub-polar North
19 Atlantic. An interplay between a weakening overturning circulation and a strengthening sub-polar
20 gyre as a consequence of 20th century global warming is identified as driving mechanism for the
21 pronounced warming along the Atlantic Water path toward the Arctic. Simulations covering the late
22 Holocene provide a reference frame that allows us to conclude that the changes during the last
23 century are unprecedented in the last 1150 years and that they cannot be explained by internal
24 variability or natural forcing alone.

26 **1 Introduction**

27 The Arctic is one of the regions where climate change has been diagnosed most drastically in terms
28 of warming and sea-ice decline over the last decades. Direct temperature measurements are,
29 however, scarce and only available for the last century. Reliable observations of sea-ice evolution are
30 even more limited, covering only the satellite era. On decadal timescales, internal variations can
31 substantially contribute to Arctic climate variability (Bengtsson et al., 2004; Beitsch et al., 2014) and
32 the relative role of external drivers is still under debate (Booth et al., 2012; Zhang et al., 2013). High-
33 resolution reconstructions of paleoclimatic variables over the late Holocene provide a reference
34 frame and put recent changes in context with long-term natural variations. Ongoing efforts, such as
35 the Past Global Changes 2K network (PAGES2K, Ahmed et al. 2013) initiative, provide regional
36 syntheses of reconstructions that can be compared with model simulations. While most of the
37 PAGES2K reconstructions rely on terrestrial proxies, high-quality marine paleodata become
38 increasingly available at annual to decadal resolution. Novel proxies have been developed to
39 reconstruct, for example, dynamical quantities such as near-bottom flow strength in the Nordic Seas
40 overflow regions (e.g., Mjell et al. 2014). Of particular value are reconstructions from key locations,
41 such as major conduits of the large-scale ocean circulation. Spielhagen et al. (2011) and Dylmer et al.
42 (2013) have published records from marine sediments off Svalbard that reflect temperature changes
43 in the Atlantic Water (AW) in Fram Strait over the last 2000-3000 years. The time series show
44 centennial-scale modulations of the AW temperatures and, as a pronounced common feature, a
45 dramatic, unprecedented warming over the 20th century. The authors speculate that the observed
46 warming reflect considerable changes in the lateral heat transfer to the Arctic that might have
47 contributed to the rapid warming and sea-ice decrease during the 20th century.

48 Earth system model simulations over the last millennium provide a tool to test such hypotheses, and
49 to investigate the relative role of internal variability on the one hand, and natural and anthropogenic
50 forcing on the other hand. Provided that the model adequately simulates regional-scale features,
51 simulations also allow for attributing locally observed variations to changes in large-scale dynamics.

52 In general, the model results have to be confronted with observations and reconstructions to assess
53 in how far they reproduce the real climate evolution, both in direct comparison (e.g., Fernandez-
54 Donado et al. 2012) and in a statistical sense (Bothe et al., 2013). In this paper, we use the results of
55 Max Planck Institute Earth System Model (MPI-ESM) simulations for the last millennium and the
56 industrial period to address the following research questions:

- 57 1. Can the simulations reproduce important features of reconstructed climate indicators in high
58 northern latitudes during the last millennium and in the 20th century, both on a continental
59 and local scale?
- 60 2. How exceptional is the observed 20th century AW warming in Fram Strait in the context of
61 the climate evolution during the last millennium, and what implications does it have for the
62 heat transfer to the Arctic?
- 63 3. What are the mechanisms behind the observed and reconstructed changes?

64 Regarding the latter, we concentrate in this paper on the 20th century changes in high northern
65 latitudes and the North Atlantic and devote a subsequent study to pre-industrial variations and their
66 relation to external forcing. The paper is organized as follows. In section 2, we describe the MPI-ESM
67 model set-up and the boundary conditions applied for the simulations covering the last millennium.
68 Results for integrated high-northern latitude changes and the evolution of the Atlantic Water
69 transfer from the North Atlantic to the Arctic are given in section 3. In section 4, we formulate a
70 dynamical interpretation of the results and discuss implications for 20th century climate change in the
71 North Atlantic realm in section 5. Main conclusions are given in section 6.

72

73 **2. The Model system and the experimental design of the last millennium simulations**

74 The model employed in this study is the Max Planck Institute Earth System Model (MPI-ESM). MPI-
75 ESM and its various configurations contributing to the Coupled Model Intercomparison Project,
76 phase 5 (CMIP5), have been documented in a special issue of the Journal for Advances in Modeling
77 Earth Systems (JAMES). The configuration for Paleo applications (MPI-ESM-P) used here is identical

78 with the MPI-ESM-LR configuration described in the JAMES publications by Giorgetta et al. (2013)
79 and Jungclaus et al. (2013) with two exceptions: First, the dynamic vegetation module is switched off
80 in order to allow for the implementation of land-cover change maps (Pongratz et al. 2008) as in the
81 earlier, lower-resolution model version described by Jungclaus et al. (2010). Second, the orbital
82 forcing is prescribed by a table providing annual values for eccentricity, obliquity and perihelion,
83 whereas the LR version uses a calendar-based orbit. The atmosphere model ECHAM6 (Stevens et al.
84 2013) is run at a horizontal resolution of spectral truncation T63 (1.875°) and 47 vertical levels,
85 resolving the stratosphere up to 0.01 hPa. The ocean/sea-ice model MPIOM (Marsland et al. 2003;
86 Jungclaus et al. 2013) features a conformal mapping grid with nominal 1.5° resolution and 40 vertical
87 levels (GR1.5L40). It is noteworthy for our study that the GR1.5L40 grid possesses one grid pole over
88 Antarctica and one grid pole over Greenland, which leads to considerably higher resolution in the
89 regions of interest for this study, i.e. the northern North Atlantic (Jungclaus et al. 2008). In Fram
90 Strait, for example, the grid size in cross-channel direction is about 30-40 km. The simulations over
91 the last millennium (past1000) follow the protocol of the Paleo Modeling Intercomparison Project,
92 phase 3 (PMIP3). As part of this protocol, Schmidt et al. (2011) summarize different choices for
93 external forcing and boundary conditions and provide tables for well mixed-greenhouse gases (CO₂,
94 CH₄, N₂O), and orbital parameters. In contrast to the millennium simulations described in Jungclaus
95 et al. (2010), which featured an interactive carbon-cycle and prognostic CO₂, we use prescribed CO₂
96 in the past1000 runs analyzed here. We employed the Crowley and Unterman (2013) reconstruction
97 for volcanic aerosol optical depth and effective radius and the Pongratz et al. (2008) reconstruction
98 of global land-cover and agricultural areas. For solar radiation we have followed the approach
99 described in Schmidt et al. (2011) combining the Vieira et al. (2011) total solar irradiance (TSI)
100 reconstruction over the Holocene with the Wang et al. (2005) data set that provides the
101 recommended solar forcing for the CMIP5 20th century (1850 – 2005) simulations. An artificial 11-yr
102 cycle of varying amplitude is imposed over the pre-industrial period (see Schmidt et al., 2011 for
103 details). Linear interpolation was used to calculate monthly TSI averages from the reconstructed

104 annual TSI values for the period 850-1849 scaled to Total Irradiance Monitor (TIM) data, except for
105 the flux at 180.5 nm. Spectral Solar Irradiance (SSI) for the 14 short-wave spectral bands of the
106 ECHAM6's radiation scheme was calculated so that the sum of SSI yields TSI. Energy in the part of the
107 spectrum below the shortest wavelength of the radiation scheme (200nm) and above the longest
108 (12195.1 nm) was added to the first and last band, respectively. Monthly average ozone
109 concentrations for the period 850-1849 are calculated using the 1850-1860 monthly climatology of
110 ozone concentrations from the AC&C/SPARC Ozone Database as a basis and representing the ozone
111 dependency on solar irradiance through regression coefficients between historical ozone
112 concentrations and the annual 180.5 nm solar flux. An 1155 year-long pre-industrial control
113 integration (PiCtrl) under fixed 1850 boundary conditions serves as a reference simulation for forced
114 experiments. To conduct the past1000 simulations we first ran a 400 year-long adaptation simulation
115 starting from the end of piCtrl to adjust to 850 boundary conditions and thereafter started the three
116 realizations past1000-r1, past1000-r2, and past1000-r3. The past1000-r1 and past1000-r2
117 experiments were initialized with the same ocean state, but differ in the standard deviation of the
118 assumed lognormal distribution of the volcanic aerosol size (1.2 μm in r1, 1.8 μm in r2 and r3). The
119 simulations past1000-r2 and past1000-r3 used the same parameter setting but were started from
120 different initial conditions. Furthermore, ozone concentration data used in past1000-r1 are affected
121 by use of a 1-month-shifted annual cycle in the AC&C/SPARC ozone climatology, an issue solved in
122 past1000-r2 and -r3. While the three simulations are therefore not an ensemble of three runs
123 carried out with an identical model and forcing/boundary conditions, we consider the effect of the
124 different setting small enough to regard the runs as three realizations of possible last millennium
125 climate evolution under parameter and forcing uncertainties. The PMIP3 protocol defines the
126 past1000 integration period as 850-1849. To relate the recent climate evolution to the late-Holocene
127 variability we continued the respective past1000 simulations over the historical period (1850 – 2005).
128 The applied boundary conditions follow the CMIP5 protocol, except for land-cover-changes, where
129 we continue the simulations with the Pongratz et al. (2008) data set. In the following, we refer to the

130 combined past1000 and historical simulations covering the period 850-2005 as pr1, pr2, and pr3,
131 respectively. Since the emphasis of our present study is on the 20th century changes, we also include
132 in some analyses in section 4 and 5 one additional MPI-ESM-P “historical” (hr1) simulation (1850-
133 2005), which was initialized from the PiCtrl experiment.

134

135 **3. Last millennium evolution of high northern latitude climate**

136 **3.1 Pan-Arctic temperature and sea-ice extent**

137 We start the analyses with quantities that reflect the general climate evolution in high northern
138 latitudes. Reconstructing regional-scale temperature and other climate variables such as sea-ice
139 extent in sparsely-sampled areas is still challenging. Only recently pan-Arctic reconstructions for
140 temperature have been published (Kaufman et al., 2009; Shi et al. 2012), mostly based on terrestrial
141 proxies (tree-rings) and ice cores. The PAGES2K consortium reviewed reconstruction data and
142 methods and constructed seven continental-scale temperature records, including the Arctic (Ahmed
143 et al. 2013). The reconstructed temperature records (black lines in Figure 1 a) have in common that
144 they show a gradual cooling during the last millennium, possibly reflecting the overall evolution from
145 a warmer Medieval Warm Period (MWP) to an anomalously cold Little Ice Age (LIA). Note that the
146 PAGES2K record reflects annual mean temperatures whereas the other two represent the summer
147 season. All reconstructions (and the instrumental data that they are matched to) show a strongly
148 reversed trend during the 20th century. The Shi et al. (2012) and Kaufman et al. (2009) summer
149 temperature reconstructions disagree on the magnitude of the pre-industrial cooling. This reflects
150 differences in the proxies chosen, their geographical distribution, and the statistical methods used to
151 match the proxies to historical observations. We are not in a position to judge which of the two time
152 series reflects more appropriate the real climate evolution; we therefore regard the discrepancy as a
153 measure of uncertainty in reconstructed climate. The simulated summer temperatures are
154 compatible with the reconstructions and match closely the Kaufman et al. (2009) data. Individual
155 simulations (colored lines in Figure 1 a) show relatively strong fluctuations and ensemble realizations

156 differ often quite strongly (about 0.5°C) for a given period. In contrast to global and hemispheric
157 averages (not shown here, but see Figure 5 in Jungclaus et al. 2010), individual volcanic eruptions
158 (like the very strong 1258 or 1453 tropical eruption) or clusters of volcanic events are not clearly
159 discernible, with the exception of the 1809 and 1815 (Tambora) eruptions, where all simulations
160 show a similar cold excursion, in accordance with the Kaufman and Past2K reconstructions. The
161 resilience to volcanic forcing reflects the relatively small signal-to-noise ratio of Arctic summer
162 temperatures, due to both strong internal variability of the Arctic regional climate (e.g. Beitsch et al.,
163 2014) and seasonal character of local response mechanisms, which are most prominent in boreal
164 winter (e.g., Zanchettin et al., 2012). Zanchettin et al. (2013) have also highlighted the role of
165 background conditions (e.g. during the closely following 1809 and 1815 eruptions) for the actual
166 response patterns, in particular at high latitudes. The Arctic warming throughout the 20th century is
167 also well reflected in the model simulations and the pronounced variations such as the warm phase
168 in the first half of the last century are well within the ensemble range of the historical experiments.
169 The summer sea-ice reconstruction by Kinnard et al. (2011) comes with a relatively large range of
170 uncertainty (dashed black lines in Fig. 1b) but the main characteristic is that of a mirror-image of the
171 pan-Arctic surface temperature evolution: A gradual increase in sea-ice extent during the pre-
172 industrial millennium is replaced by a drastic decline in the 20th century (Figure 1 b). The decline of
173 sea-ice extent sets in, however, more abruptly in the mid-20th century in contrast to the relatively
174 gradual warming. The past1000 simulations reproduce a similar long-term trend over the pre-
175 industrial millennium and the 20th century simulations terminate at an extent that is equally low as
176 the observations. In the simulations, the sea-ice decline begins, however, earlier featuring a temporal
177 evolution more similar to the pan-Arctic temperature (Figure 1a). In fact, all four historical
178 simulations show ice extent anomalies below the reconstruction's mean estimate between 1870 and
179 1950. The sea-ice reconstruction exhibits a pronounced relative minimum in the late 16th century,
180 which none of the three past1000 simulations reproduces. Notwithstanding questions regarding
181 uncertainties in the reconstructions, it is difficult to relate the event to known volcanic or solar

182 forcing variations (e.g. the minimum around 1700 appears at the time of the Maunder minimum in
183 solar variations). The anomalies in the 15th to 17th century exceed the 2-sigma range of control
184 experiment variability significantly. We have detected events of similar magnitude in unforced
185 control simulations, but they appear only rarely (once in a 1000-yr simulation). It is therefore
186 possible that the model underestimates internal variability of the sea-ice extent.

187

188 **3.2 Fram Strait Atlantic Water temperatures**

189 The reconstructions of AW temperatures stem from a marine core at site MSM5/5-712 at
190 78°54.94'N, 6°46.04'E (see Spielhagen et al. (2011) and Werner et al. (2011) for details). The authors
191 provide two temperature records, one based on a modern analogue technique (SIMMAX), and one
192 based on the Magnesium-Calcium (Mg/Ca) ratio of *Neogloboquadrina pachyderma*. Habitat and
193 plankton bloom estimates indicate that both proxies reflect mid-summer conditions in the upper part
194 of the AW layer. During pre-industrial times, the Mg/Ca-derived record exhibits much stronger
195 variability, which might reflect inaccuracies in recording the cold-water range (Spielhagen et al.,
196 2011). Both reconstructions, however, fluctuate around very similar pre-industrial mean values (3.4°
197 and 3.6°C) and indicate a warming of roughly 2°C during the 20th century (Figure 2). A similar
198 temperature increase is also found in continued measurements from Svalbard fjords from 1912 to
199 2005 (Pavlov et al., 2013) and agrees with previous estimates of 20th century evolution of AW
200 properties in the northern North Atlantic (Polyakov et al., 2004). Another late-Holocene sedimentary
201 record from Malangen Fjord in northern Norway (Hald et al. 2011) reflects local variations in the
202 influx of AW and shows a similar temperature evolution over the last 1200 years including an
203 unprecedented warming in modern times.

204 We compare the Spielhagen et al. (2011) reconstructions with simulated fluctuations of
205 temperatures in the AW core at 50m depth in Fram Strait at about 78°N (Figure 2). The relatively low
206 temporal resolution and the strong fluctuations in the Mg/Ca record prohibit a very detailed
207 comparison in the pre-industrial millennium. The simulations and the SIMMAX data agree in a change

208 from slightly warmer-than-average temperatures in the first centuries and colder conditions in the
209 16th to 18th centuries, reflecting the general change from MWP to LIA conditions. Interestingly, all
210 time-series show a cold spell in the early 19th century, likely recording the 1809 and 1815 eruptions.
211 During the 20th century, simulations and the SIMMAX record agree in a 2°C warming. The simulations
212 also exhibit considerable decadal to multidecadal variations that are not covered or sub-sampled by
213 the reconstructions' resolution. The ensemble spread and the relatively large variability range
214 obtained from the unforced control run (Figure 2), points to a large fraction of internal variability.
215 Clearly, the warming in the industrial period exceeds the 2 σ -range of the undisturbed simulation.
216 Spielhagen et al. (2011) speculate that the diagnosed warming infers a considerable increase in heat
217 transfer to the Arctic. In the model simulations, we can quantify the heat flux changes and display in
218 Figure 3a the combined total ocean heat transport (TOHTR) through Fram Strait and through the
219 Barents Sea Opening (BSO), which both show the unprecedented increase in the 20th century. Firstly,
220 we confirm that the AW temperature record reflects indeed changes in heat transfer through the
221 most important conduits towards the Arctic. The correlation coefficients between AW temperatures
222 and TOHTR (smoothed by a 31-yr running mean) exceed 0.9 at zero time-lag in all three past1000
223 simulations. Simulated TOHTR anomalies are shown with respect to (w.r.t.) the pre-industrial (850-
224 1849) mean of about 80 TW (1 TW = 10¹² Watt). The simulated transports are compatible with
225 observations indicating a heat transport of 30-40 TW in Fram Strait (Schauer et al., 2008) and 30-76
226 TW in BSO (Årthun et al., 2012). Observations of heat transports are, however, only available for the
227 most recent decades and may be influenced by decadal-scale variability as well. During the pre-
228 industrial period, there are TOHTR fluctuations of the order of 10-20 TW and the ensemble indicates
229 somewhat higher-than-normal TOHTR in the early part of the simulation and less TOHTR in the 16th
230 and 17th century. Large volcanic eruptions (1258, 1453, and 1815) leave an imprint on the heat
231 transports leading to reduction of heat transfer to the Arctic (Zanchettin et al., 2012). The most
232 pronounced feature of our smoothed time series from the simulations is, however, a consistent

233 increase of up to 30 TW during the 20th century, reflecting a 40% increase over the pre-industrial
234 mean.

235 The modulation of the AW temperature could either be driven by local changes in the wind system
236 (Bengtsson et al., 2004) or be part of variations in the warm water path associated with the North
237 Atlantic Current or the Atlantic Meridional Overturning Circulation (AMOC), as has been suggested,
238 for example by Polyakov et al. (2004). However, recently Lozier (2010) and Lozier et al. (2010) have
239 demonstrated that overturning and gyre circulation in the North Atlantic are strongly linked and that
240 the image of a continuous conveyor belt associated with the AMOC may be misleading. Building on
241 earlier results analyzing Arctic warming events in an unperturbed control integration (Beitsch et al.,
242 2014) we therefore decompose the (TOHTR) in the Atlantic basin into its overturning and gyre
243 components (MOHTR, and GOHTR, respectively). The first reflects the zonal average heat transport,
244 the second the deviations of the zonal average (e.g. Eden and Jung, 2001; Drijfhout and Hazeleger,
245 2006). First, we calculate the correlations between the TOHTR at the entrance to the Arctic (Figure
246 3a) and the components of the basin-scale OHTRs for all latitudes. High correlations are found in
247 particular in the sub-polar North Atlantic between GOHTR and heat transfer to the Arctic (not
248 shown). At the entrance to the Nordic Seas at 60°-65°N (Figure 3b) we can see that most of the
249 modulation in the heat transfer to the Arctic during the millennium can be traced back to downstream
250 fluctuations in GOHTR. The gyre heat transport features multi-centennial changes from stronger-
251 than-normal conditions in the early centuries of the simulation to weaker conditions during the Little
252 Ice Age. The 20th century stands out again with its unprecedented increase in the TOHTR. Most of the
253 increase at 60-65°N is carried by an increase in the gyre component, but, interestingly, also the
254 overturning component shows a clear positive trend over the 20th century and apparently
255 contributes to high-latitude warming despite the fact that AMOC is decreasing at 30°N over the 20th
256 century.

257

258 **4. Origin of the 20th century heat transfer increase**

259 In the following, we focus on the changes in the 20th century and elucidate the relation between heat
260 transfer changes in Fram Strait and the sub-polar North Atlantic. We consider simulated linear 100yr
261 trends (1905-2005) and compare them with the expected range of internal variability as expressed in
262 the 5-95 percentile range of the respective variables taken from the 1000 yr-long PiCtrl simulation.

263 The changes in the heat transport components over the 20th century reflect trends in the large-scale
264 ocean circulation. Figure 4 shows the centennial trends for the AMOC streamfunction (Figure 4a) as
265 function of latitude and for the barotropic horizontal streamfunction (Figure 4b) together with their
266 long-term means. The AMOC increases at higher-latitudes, but the most prominent feature is a
267 broad-scale weakening in subtropical and subpolar latitudes at depth below 1000m. As has been
268 described in previous studies (e.g. Latif et al., 2006), this weakening is associated with reduced deep-
269 water formation, most prominently in the Labrador Sea (see below). On the other hand, the
270 circulation cell reaching into the Nordic Seas strengthens as more overturning occurs at higher
271 latitudes. The barotropic streamfunction trends are characterized mainly by a pronounced
272 strengthening (the negative sign refers to more cyclonic circulation) in the central and eastern part of
273 the subpolar basin. In the central Labrador Sea, the gyre circulation weakens, which is, again,
274 compatible with reduced deep water formation in the main convection region. There is also
275 indication of a weakening of the gyre circulation in the Nordic Seas.

276 The change in TOHTR in the Atlantic basin reflects the trends in its components: in particular in sub-
277 polar latitudes, a weaker overturning component is mostly compensated by a stronger gyre
278 component (Figure 5a), but the resulting TOHTR does not exceed the range of internal variability.
279 North of 55°N changes in both components are much smaller, but are constructively adding up to
280 positive TOHTR trends. The trends are robust in the four simulations, and the 20th century TOHTR
281 trends exceed the 5-95% range deduced from the PiCtrl run in three of the four simulations. In
282 subtropical latitudes, overturning transports are also smaller, but not compensated by the gyre
283 transports. Thus the TOHTR here are considerably weaker and exceed the 5-95% range of trends in
284 the control simulation. Meridional divergence or convergence of TOHTR then causes regional cooling

285 or warming, if not compensated by surface heat fluxes. Therefore, positive slopes of the TOHTR
286 curves in Fig. 5a indicate cooling while negative slope indicate warming, as indicated by the red and
287 light-blue horizontal lines at the bottom of Figure 5aa. Regions, where divergence of advective lateral
288 heat transport cools the ocean (Figure 5a) are associated with positive atmosphere-ocean heat flux
289 trends, indicating that the colder ocean is cooling the atmosphere. Hence the atmosphere is damping
290 the ocean-induced changes rather than enforcing them. Trends in the upper-ocean temperatures are
291 negative roughly between 45° and 60°N and, since they are only partly compensated by freshening
292 (not shown), there are considerable changes in the density structure as is shown for the pr2
293 experiment in Figure 6 (results are similar for all simulations). Increased density in the center and
294 more pronounced doming of the subpolar isopycnals is typical for a strengthening gyre. The
295 increasing horizontal density gradients, on the other hand, indicate higher baroclinic pressure
296 gradients and further accelerate the gyre (Greatbatch et al., 1991; Levermann and Born, 2007).

297 A possible reason for the acceleration of the gyre circulation could be changes in the wind system.
298 Modulations of large-scale atmospheric pressure patterns like the North Atlantic Oscillation or the
299 East Atlantic Pattern leave their specific imprint on the wind-driven ocean circulation (Häkkinen and
300 Rhines, 2009) and may be important also on centennial time scales (e.g., Sedláček and Mysak, 2009).

301 In particular, the gyre would respond to changes in the wind-stress curl caused, for example, by a
302 poleward shift of the westerlies due to global warming (e.g. Saenko et al., 2005). The centennial
303 trends in the zonal wind stress component are indeed relatively coherent in the past1000
304 experiments and resemble those obtained by Saenko et al. (2005) in idealized CO₂-doubling
305 experiments: stronger positive wind stress north of 40°N and slightly negative values in the sub-
306 tropical region (Figure 7a). While consistent in three of the four experiments considered here, the
307 changes are well within the 5-95%tile range obtained from the unperturbed control experiment.

308 Moreover, trends in wind-stress curl (Figure 7b) indicate coherent changes only in the Southern
309 Hemisphere (not shown), which is, again, consistent with the findings by Saenko et al. (2005), who
310 applied somewhat stronger CO₂ forcing.

311
312
313
314
315
316
317
318
319
320
321
322
323
324
325
326
327
328
329
330
331
332
333
334
335
336

To further elucidate the origin of the circulation changes we identify first the reason for the weakening of the AMOC in the subtropical and subpolar North Atlantic. A key ingredient modulating the AMOC here is the strength of deep water formation in the Labrador Sea (Latif et al., 2006; Lohmann et al., 2014). To quantify the latter we calculate the thickness of the Labrador Sea Water (LSW) in the region (for details, see Lohmann et al., 2014). Normalizing the anomalies, we see a clear co-variability with the AMOC at 30N and 1500m depth when AMOC lags by roughly 8-10 years. Next, we establish a link between LSW thickness and surface properties by correlating LSW thickness with the surface density field (not shown), which reveals the central Labrador Sea as convection hot-spot. The evolution of surface density, temperature and salinity in the so-identified region reveals, as expected, that enhanced LSW formation comes together with positive density anomalies at the surface that reduce the static stability and induce convection. Also shown in Figure 8a are the corresponding temperature and salinity time series. Following the evolution through the last three centuries indicate pronounced multi-decadal variability and pronounced differences between the industrial period and the centuries before. The multidecadal variability is characterized by co-varying temperature and salinity, where apparently, density is determined by the salinity changes (e.g., fresher and lighter conditions lead to less dense surface waters, which is not compensated by colder temperatures). The variations in the regional fresh-water budget is mainly caused by modulations of the sea-ice and fresh water supply from higher latitudes (Jungclaus et al., 2005) and from redistribution of zonal salinity transport by the Irminger Current. During the 20th century, however, this relation breaks down as somewhat fresher conditions (also caused by increasing sea-ice and fresh-water export through Denmark Strait, not shown) go along with a general warming, partly caused by direct radiative forcing, partly by redistribution of heat by an enhanced Irminger Current. As a result, AMOC weakens at latitudes downstream from the LSW formation region. The temporal evolution of the vertical density structure in the Labrador Sea indicates then generally less dense

337 conditions in the upper 2000m. Interestingly, the deepest layers are characterized by relatively
338 colder temperatures and higher densities that are caused by the enhanced overturning in the Nordic
339 Seas and associated changes in the strength and density of the Denmark Strait overflow. Changes in
340 the vertical density structure are important for the east-west density gradient driving the AMOC
341 (Lozier et al., 2010), but also affect the baroclinic structure of the gyre directly (Drijfhout and
342 Hazeleger, 2006).

343

344 **5. Discussion**

345 Our analysis has demonstrated that the increasing heat transports to higher latitudes are mainly
346 caused by changes in the gyre and overturning circulation in the subpolar North Atlantic. These
347 changes are caused by a reduction in deep water formation in the Labrador Sea, which leads to
348 reduced overturning circulation in subtropical and subpolar latitudes. In addition, changes in the
349 vertical structure of water masses at the western boundary can modify the baroclinic gyre circulation
350 (Drijfhout and Hazeleger, 2006). The associated changes in MOHTR and GOHTR lead to enhanced
351 TOHTR towards higher latitudes and heat transport divergence (cooling) in the subpolar region.⁵ The
352 colder and denser SPG then spins up baroclinically, which further increases the GOHTR (dashed lines
353 in Figure 5a), which, in turn, extracts even more heat from the SPG center and further increases the
354 horizontal density gradient. Thus a positive feedback mechanism is initiated. The mechanism can be
355 compared to the one described by Levermann and Born (2007) and Born et al. (2013a). These
356 authors describe a positive feedback, where an (somehow) accelerated gyre leads to increasing east-
357 west temperature and salt transports along its northern rim. Increasing salinity then leads to denser
358 surface waters in the Labrador Sea and to enhanced convective activity, which further spins up the
359 gyre. In our simulations, we see also a redistribution of salinity during the 20th century change in gyre
360 circulation resulting in higher salinities in the western part of the basin. However, in contrast to the
361 mechanism described by Levermann and Born (2007), the positive temperature anomalies dominate
362 the near-surface density evolution in the industrial period and Labrador Sea convection rather

363 decreases. Levermann and Born (2007) demonstrated that a bistability regime exists, where the
364 transition between the two regimes can be triggered by small fluctuations in surface freshwater flux.
365 Born et al. (2013a) extended the study and found multiple circulation modes in PiCtrl experiments in
366 six out of 19 models (among them MPI-ESM-LR). Even though we find some differences to their
367 mechanism, it is possible that the relatively strong response of the SPG is an expression of such a
368 transition, here triggered by changes in the AMOC. Possibly also the wind-stress changes (Figure 7)
369 play a role in initiating the change in the gyre circulation by modified Ekman and/or Sverdrup
370 transports. Furthermore, gyre circulation changes can also directly be driven by changes in the
371 baroclinic structure at the western boundary as has been shown in the global warming simulations by
372 Drijfhout and Hazeleger (2006). At the western boundary near the exit of the Labrador Sea (Figure
373 8b), the density changes are consistent with a weakening of Labrador Sea Water production and an
374 increase in overflow-derived density, similar to what has been found by Drijfhout and Hazeleger
375 (2006). It is difficult, however, to exactly detect which component is more important in initially
376 triggering the mechanism. For this, additional sensitivity experiments (e.g., partial-coupling
377 experiments) would be necessary, which is beyond the scope of this study. In any case, an important
378 ingredient is the weakening of the AMOC in subtropical and subpolar latitudes, caused by a decrease
379 in Labrador Sea Water formation as a response to global warming, while the deep water production
380 in the Nordic Seas is even slightly enhanced. The exact mechanisms of how gyre and overturning
381 circulations interact are also difficult to disentangle. In the historical simulations, changes in AMOC
382 and SPG circulation appear to happen more or less instantaneous, whereas analyses of the
383 unperturbed control simulation suggest that AMOC variations are leading by a few years.

384 Many CMIP5 models feature a reduction of the AMOC strength already in the 20th century (Drijfhout
385 et al., 2012). A characteristic feature of these simulations is the “warming hole” above the sub-polar
386 North Atlantic that can also be identified in observations (e.g. in the HadSST data set; Rayner et al.,
387 2006). A cool surface temperature spot within the intensified SPG is also characteristic for our 20th
388 century simulations (Figure 6) and related to the mechanism described above. Drijfhout et al. (2012)

389 decompose the temperature pattern in a radiatively forced and an AMOC fingerprint and conclude
390 that the cold sub-polar North Atlantic is indeed related to an AMOC decline. Kim and An (2012) come
391 to a similar conclusion analyzing CO₂-doubling experiments from the Coupled Model Intercomparison
392 Project Phase 3 data base.

393 Another indication that the mechanism described here is at work in reality comes from
394 paleoceanographic reconstructions for the late Holocene. Miettinen et al. (2012) compare the
395 temporal evolution of ocean temperatures at two locations, the Voering Plateu in the Norwegian Sea
396 and the SPG region south of the Reykjanes Ridge. They find that low-frequency fluctuations occur
397 out-of-phase: the Voering Plateau record features, for example, a cold anomaly during the Little Ice
398 Age (LIA), whereas the SPG is warmer than normal during this period. Such a behavior is compatible
399 with the findings described here: A weaker SPG in the LIA (Figure 3) would feature a less dense and
400 warmer center (opposite to what is seen for the strong-gyre anomaly in Figure 6) and would
401 transport less heat to the Nordic Seas. Such out-of-phase anomalies of the barotropic stream
402 function in the SPG region and the Nordic Seas can also be seen in Figure 4b. A detailed investigation
403 of the variations and processes during the pre-industrial millennium and their relation to natural
404 forcing will be subject of a subsequent study.

405 Obtaining a comprehensive view from long-term direct observations of temperature, salinity, or
406 transports remains challenging. There exist only a few long-term time series. Many continuous
407 records, such as those from weather ships (e.g. Østerhus and Gammelsrød, 1999) cover the last
408 decades and are characterized by multi-decadal variability. The temperature measurements over the
409 20th century near Svalbard by Pavlov et al. (2013) and one of the longest time-series available at all,
410 the Kola section in the Barents Sea (e.g., Skagseth et al., 2008) support the pronounced warming in
411 the Atlantic Water branch in the industrial period. Polyakov et al. (2004) synthesized various
412 observational data sets to conclude that the intermediate Atlantic Water layer in the Arctic shows a
413 continuous warming trend that is superposed by multi-decal variability. Combining proxy data and
414 observations, Cunningham et al. (2013) compiled a synthesis of SST changes in the north-eastern

415 North Atlantic and the Nordic Seas during the last millennium. For the 20th century (their Figure 1a),
416 they report that most of the records reflecting the Atlantic Water branch along Scotland and Norway
417 indicates a warming, while other records from the sub-polar North Atlantic indicate neutral or
418 cooling conditions. High-resolution proxies from the Iceland Basin (Hall et al., 2010) over the last 230
419 years indicate cooling of SSTs in the central subpolar gyre region, which would be consistent with our
420 findings. The available SST gridded data sets HadISST (Rayner et al., 2006) and ERSSTv3 (Smith and
421 Reynolds, 2004) as well as the Simple Ocean Data Assimilation (SODA) reanalysis (Carton and Giese,
422 2008) are all characterized by a cooling trend in the subpolar gyre region (Drijfhout et al., 2012; Kim
423 and An, 2012). Polyakov et al. (2010) have used historical data from the North Atlantic Ocean and
424 decomposed the changes between the 1920s and present into non-linear trend and multi-decadal
425 variability patterns. The large-scale nonlinear trend pattern resembles the 20th century SST trend in
426 the HadISST and is characterized by cooling over the subpolar gyre (see their figure 5) and warming in
427 the subtropical North Atlantic and on the northwestern European Shelf, again compatible with our
428 results for the 20th century simulations. On the other hand, the 20th century compilation of
429 temperature and salinity data from the subpolar gyre region by Reverdin (2010) compares less well
430 with our study: the central SPG at about 60N is characterized by slightly positive temperature and
431 negative density trends.

432 Uncertainties in early observations and reconstructions preclude a definite answer to what degree
433 the findings reported here can be verified by observations. While the dynamical mechanisms
434 proposed here to explain the enhanced heat transfer to the Arctic appear largely compatible with
435 observed features in the North Atlantic, they may depend on the particular model system. Moreover,
436 as many other CMIP5 models, MPI-ESM features large SST and circulation biases in the North
437 Atlantic. In particular, the path of the Gulf Stream/North Atlantic Current is too zonal (Jungclaus et
438 al., 2013), which has direct consequences for the shape of the gyres. This may affect the warm water
439 path from the Subtropics to the Nordic Seas. Using observations and model simulations for the
440 second half of the 20th century, Hatún et al. (2005) concluded that a weaker (and less zonally-

441 extended) SPG would allow more warm and saline water to enter the Nordic Seas. Our simulations,
442 but also other CMIP5 ESMs (Born et al., 2013a; Koenigk and Bradeau, 2014) and stand-alone ocean
443 model simulations with the same ocean model as used here, but forced by reanalysis data (Müller et
444 al., 2014) suggest that a stronger SPG carries more subtropical AW into the Nordic Seas and the
445 Arctic. This discrepancy may be related to the specific situation of the late 20th century described by
446 Hatún et al. (2005), where SPG changes were mainly related to the atmospheric forcing (Häkkinen
447 and Rhines, 2009; see also Born et al., 2013b).

448 A 30 TW increase in heat transfer to the Arctic over 100 years as suggested by our simulations for the
449 20th century is an important contribution to the Arctic heat budget (Serreze et al., 2007). Dividing by
450 the area of the Arctic, it corresponds to a substantial forcing of about 2 Wm⁻². Jungclaus and Koenigk
451 (2010) and Beitsch et al. (2014) have shown that multidecadal variations in TOHTR to the Arctic
452 impact the Arctic climate. For positive TOHTR anomalies, the sea-ice cover decreases most
453 pronounced in the Barents Sea and causes considerable variations in ocean-atmosphere heat fluxes.
454 Although only a small fraction of the Arctic is affected, the associated warming leads to positive pan-
455 Arctic temperature anomalies. Moreover, the heat-flux changes affect the atmospheric circulation.
456 An associated feedback mechanism is the Bjerknes Compensation (Bjerknes, 1964; Shaffrey and
457 Sutton, 2006; Jungclaus and Koenigk, 2010): on multidecadal time-scales, TOHTR and atmospheric
458 heat transports (AHTR, here derived from the components of moist and dry static energy advection
459 following Keith (1995)) are strongly coupled and may compensate each other. Thus, both TOHTR and
460 AHTR need to be considered for an assessment of the lateral heat transfer changes as part of the
461 Arctic heat budget. Comparing TOHTR and AHTR at 70°N (Figure 9) indicates considerable
462 multidecadal variability, where the respective TOHTR and AHTR tend to evolve out-of-phase.
463 However, there is no compensation of the strong positive trend in TOHTR during the last decades of
464 the simulation. Therefore we conclude that there is a net positive contribution from the lateral heat
465 fluxes to the Arctic heat budget and to the warming in recent decades. An assessment of all terms of
466 the Arctic heat budget and the feedback mechanisms leading to Arctic Amplification is, however,

467 beyond the scope of our paper. The magnitude of TOHTR changes appears to play a decisive role in
468 the amplitude of pan-Arctic warming, and sea-ice evolution in climate-change simulations (Mahlstein
469 and Knutti, 2011). These authors concluded that the TOHTR changes contribute significantly to Arctic
470 amplification, but they also identified considerable differences in the TOHTR magnitude in the
471 CMIP3-model suite as a cause for model uncertainty in projected Arctic warming.

472

473 **6. Conclusions**

474 The MPI-ESM last-millennium simulations consistently reproduce enhanced 20th century warming of
475 AW at the boundary between the Nordic Seas and the Arctic compared with pre-industrial variability.
476 The warming of AW in Fram Strait is an indicator for a prominent (~40%) increase in oceanic heat
477 transfer to the Arctic during the 20th century. In the simulations, we are able to trace back the heat
478 transport changes to a reorganization of the large-scale ocean circulation in the sub-polar North
479 Atlantic. The SPG and the associated northward heat transport are intensified by the global-warming-
480 induced weakening of the AMOC and changes in the density structure associated with modified deep
481 water formation. The latter also lead to a slight intensification of the overturning in high northern
482 latitudes. Together, the gyre and overturning-related heat transport changes lead to an increase in
483 the heat transfer to the Nordic Seas and the Arctic. Changes in wind-stress curl do not appear to be
484 significantly different from the unperturbed variability, but wind-stress changes may nonetheless
485 play a role in triggering the mechanism. Transient simulations over the late Holocene provide a
486 valuable reference frame to discriminate unprecedented changes such as those observed in the 20th
487 century from natural or internal fluctuations.

488

489 **Acknowledgements:** This work was supported by the European Community's 7th framework
490 program (FP7/2007-2013) under grant agreement no. 308299 (NACLIM). D.Z. was supported by the
491 German Federal Ministry for Education and Research (BMBF) Miklip project (FKZ: 01LP1158A). The
492 MPI-ESM-P simulations were conducted at the German Climate Computing Center (DKRZ). The
493 authors thank Chao Li and two anonymous reviewers for comments that helped improving the
494 manuscript. The service charges for this open access publication have been covered by the Max
495 Planck Society.

496

497

498

499 **References:**

500 Ahmed, M. and the PAGES 2k Consortium: Continental-scale temperature variability during the last
501 two millennia, *Nature Geosci.*, 6, 339–346, doi:10.1038/ngeo1797, 2013.

502 Årthun, M., Eldevik, T., Smedsrud, L.H., Skagseth, Ø., Ingvaldsen, R.B.: Quantifying the influence of
503 Atlantic heat on Barents Sea ice variability and retreat, *J. Climate*, 25, 4736-4743,
504 doi:10.1175/JCLI-D-11-00466.1, 2012.

505 Beitsch, A., Jungclaus, J.H., and Zanchettin, D.: Patterns of decadal-scale Arctic warming events in
506 simulated climate. *Clim. Dynam.*, 43, 1773-1789 doi:10.1007/s00382-013-2004-5, 2014.

507 Bengtsson, L., Semenov, V.A., and Johannessen, O.M.: The early twentieth-century warming in the
508 Arctic – a possible explanation. *J. Climate*, 18, 4045-4057, doi:10.1175/1520-
509 0442(2004)017<4045:TETWIT>2.0.CO;2, 2004.

510 Bjerknes, J.: Atlantic air-sea interaction, *Adv. Geophys.*, 10, 1-82, 1964.

511 Booth, B.B.B., Dunstone, N.J., Halloran, P.R., Andrews, T., and Bellouin, N.: Aerosols implicated as a
512 prime driver of twentieth century North Atlantic climate variability, *Nature*, 484, 228-232,
513 doi:10.1038/nature10946, 2012.

514 Born, A., Stocker, T.F., Raible, C.C., and Levermann, A.: Is the Atlantic subpolar gyre bistable in
515 comprehensive climate models? *Clim. Dynam.*, 40, 2993-3007, doi:10.1007/s00382-012-1525-7,
516 2013a.

517 Born, A., Stocker, T.F., and Sandø, A.B.: Coupling of eastern and western subpolar North Atlantic: salt
518 transport in the Irminger Current, *Ocean Sci. Discuss.*, 10, 555-579, 2013b.

519 Bothe, O., Jungclaus, J.H., and Zanchettin, D.: Consistency of the multi-model CMIP5/PMIP3
520 ensemble, *Clim. Past*, 9, 2471-2487, doi:10.5194/cp-9-2471-2013201, 2013.

521 Carton, J.A., and Giese, B.S.: A reanalysis of ocean climate using Simple Ocean Data Assimilation
522 (SODA). *Mon. Weather Rev.*, 136, 2999-3017, doi: 10.1175/2007MWR1978.1, 2008.

523 Crowley, T.J., and Unterman, M.B.: Technical details concerning development of a 1200 yr proxy
524 index for global volcanism, *Earth Syst. Sci. Data*, 5, 187-197, doi:10.5194/essd-5-187-2013, 2013.

525 Cunningham, L., Austin, W.E.N., Knudsen, K.L., Eiriksson, J., Scourse, J.D., Wanamaker, A.D. Jr., Butler,
526 P.G., Cage, A.G., Richter, T. Husum, K., Hald, M., Andersson, C., Zorita, E., Linderholm, H.W.,
527 Gunnarson, B.E., Sicre, M.-A., Sejruo, H.P., Jiang, H., and Wilson, R.: Reconstructions of surface
528 ocean conditions from the northeast Atlantic and Nordic Seas during the last millennium. *The*
529 *Holocene*, 23, 921-935, doi:10.1177/0959683613479677, 2013.

530 Drijfhout, S.S., and Hazeleger, W.: Changes in MOC and gyre-induced Atlantic Ocean heat transport,
531 *Geophys Res. Lett.*, 33, L07707, doi:10.1029/2006GL025807, 2006.

532 Drijfhout, S., van Oldenborgh, G.J., and Cimadoribus, A.: Is a decline of AMOC causing the warming
533 hole above the North Atlantic in observed and modeled warming patterns? *J. Climate*, 25, 8373-
534 8379, doi:10.1175/JCLI-D-12-00490.1, 2012.

535 Dylmer, C.V., Girardeau, J., Eynaud, F., Husum, K., De Vernal, A.: Northward advection of Atlantic
536 water in the eastern Nordic Seas, *Clim. Past*, 9, 1505-1518, doi:10.5194/cp-9-1505-2013, 2013.

537 Eden, C., and Jung, T.: North Atlantic interdecadal variability: oceanic response to the North Atlantic
538 Oscillation (1865-1997), *J. Climate*, 14, 676-691, 2001.

539 Fernández-Donado, L., González-Rouco, J.F., Raible, C.C., Ammann, C.M., Barriopedro, D., García-
540 Bustamante, E., Jungclaus, J.H., Lorenz, S.J., Luterbacher, J., Phipps, S.J., Servonnat, J.,
541 Swingedouw, D., Tett, S.F.B., Wagner, S., Yiou, P., and Zorita, E.: Large-scale temperature
542 response to external forcing in simulations and reconstructions of the last millennium, *Clim.Past*,
543 9, 393-421, doi:10.5194/cp-9-393-2013, 2013.

544 Giorgetta, M. A., Jungclaus, J. H., Reick, C. H., Legutke, S., Brovkin, V., Crueger, T., Esch, M., Fieg, K.,
545 Glushak, K., Gayler, V., Haak, H., Hollweg, H.-D., Ilyina, T., Kinne, S., Kornblueh, L., Matei, D.,
546 Mauritsen, T., Mikolajewicz, U., Mueller, W. A., Notz, D., Raddatz, T., Rast, S., Redler, R., Roeckner,
547 E., Schmidt, H., Schnur, R., Segschneider, J., Six, K., Stockhause, M., Wegner, J., Widmann, H.,
548 Wieners, K.-H., Claussen, M., Marotzke, J., and Stevens, B.: Climate and carbon cycle changes from
549 1850 to 2100 in MPI-ESM simulations for the Coupled Model Intercomparison Project phase 5, *J.*
550 *Adv. Model Earth Syst.*, 5, 1–26, doi:10.1002/jame.20038, 2013.

551 Greatbatch, R., Fanning, A., Goulding, A., and Levitus, S.: A diagnosis of interpentadal circulation
552 changes in the North Atlantic, *J. Geophys. Res.*, 96, 22,009-22,023, 1991.

553 Häkkinen, S., and Rhines, P.B.: Shifting surface currents in the northern North Atlantic, *J. Geophys.*
554 *Res.*, 114, C04005, doi:10.1029/2008JC004883, 2009.

555 Hald, M., Salomonsen, G.R., Husum, K., and Wilson, L.J.: A 2000 year record of Atlantic Water
556 temperature variability from Malangen Fjord, northeastern North Atlantic, *The Holocene*, 21,
557 1049-1059, doi:10.1177/095968361140057, 2011.

558 Hall, I.R., Boessenkool, K.P., Barker, S., McCave, N., and Elderfield, H.: Surface and deep ocean
559 coupling in the subpolar North Atlantic during the last 230 years. *Paleoceanography*, 25, PA2101,
560 doi:10.1029/2009PA001886, 2010.

561 Hátún, H., Sandø, A.B., Drange, H., Hansen, B., and Valdimarsson, H.: Influence of the Atlantic
562 subpolar gyre on the thermohaline circulation. *Science*, 309, 1841-1844,
563 doi:10.1126/science.1114777, 2005.

564 Jungclaus, J.H., Haak, H., Mikolajewicz, U., and Latif, M.: Arctic-North Atlantic interactions and
565 multidecadal variability of the meridional overturning circulation. *J.Climate*, 18, 4016-4034, 2005.

566 Jungclaus, J.H., Macrander, A., and Käse, R.H.: Modelling the overflow across the Greenland-Scotland
567 Ridge, in: *Arctic-subarctic ocean fluxes*, edited by Dickson, R.R., Meincke, J., and Rhines, P.,
568 Springer, Dordrecht, 527-549, 2008.

569 Jungclaus, J.H., Lorenz, S.J., Timmreck, C., Reick, C.H., Brovkin, V., Six, K., Segschneider, J., Giorgetta,
570 M.A., Crowley, T.J., Pongratz, J., Krivova, N.A., Vieira, L.E., Solanki, S.K., Klocke, D., Botzet, M.,
571 Esch, M., Gayler, V., Haak, H., Raddatz, T.J., Roeckner, E., Schnur, R., Widmann, H., Claussen, M.,
572 Stevens, B., and Marotzke, J.: Climate and carbon-cycle variability over the last millennium, *Clim.*
573 *Past*, 6, 723-737, doi:10.5194/cp-6-723-2010, 2010.

574 Jungclaus J.H., and Koenigk, T.: Low-frequency variability of the Arctic climate: the role of oceanic
575 and atmospheric heat transport variations. *Clim. Dynam.*, 34, 265-279, doi:10.1007/s00382-009-
576 0569-9, 2010.

577 Jungclaus, J.H., Fischer, N., Haak, H., Lohmann, K., Marotzke, J., Matei, D., Mikolajewicz, U., Notz, D.,
578 and von Storch, J.-S.: Characteristics of the ocean simulations in the Max Planck Institute Ocean
579 Model (MPIOM) the ocean component of the MPI-Earth system model, *J. Adv. Model Earth Syst.*,
580 5, 422-446, doi:10.1002/jame.20023, 2013.

581 Kaufman, D.S., Schneider, D.P., McKay, N.P., Ammann, C.M., Bradley, R.S., Briffa, K.R., Miller, G.H.,
582 Otto-Bliesner, B.L., Overpeck, J.T., Vinther, B.M., and Arctic Lakes 2K project members: Recent
583 warming reverses long-term Arctic cooling. *Science*, 325, 1236-1239,
584 doi:10.1126/science.1173983, 2009.

585 Keith, D.W.: Meridional energy transport: uncertainty in zonal means. *Tellus*, 47A, 30-44, 1995.

586 Kim, H., and S.-I. An: On the subarctic North Atlantic cooling due to global warming. *Theor. Appl.*
587 *Climatol.*, 114, 1-19, doi:10.1007/s00704-012-0805-9, 2012.

588 Kinnard, C., Zdanowicz, C.M., Fisher, D.A., Isaksson, E., De Vernal, A., and Thompson, L.G.:
589 Reconstructed changes in Arctic sea ice over the last 1,450 years. *Nature*, 479, 509-513,
590 doi:10.1038/nature10581, 2011.

591 Koenigk, T., and Brodeau, L.: Ocean heat transport into the Arctic in the twentieth and twenty-first
592 century in EC-Earth, *Clim. Dynam.*, 42, 3101-3120, doi:10.1007/s00382-013-1821-x ,2014.

593 Latif, M., Böning, C., Willebrand, J., Biastoch, A., Dengg, J., Keenlyside, N., Schweckendiek, U., and
594 Madec, G.: Is the Thermohaline Circulation Changing?. *J. Climate*, 19, 4631–4637, doi:
595 <http://dx.doi.org/10.1175/JCLI3876.1>, 2006.

596 Levermann, A., and Born, A.: Bistability of the Atlantic subpolar gyre in a coarse-resolution climate
597 model. *Geophys. Res. Lett.*, 34, L24605, doi:10.1029/2007GL031732, 2007.

598 Lohmann, K., Jungclaus, J.H., Matei, D., Mignot, J., Menary, M., Langehaug, H.R., Ba, J., Gao, Y.,
599 Otterå, O.H., Park, W., and Lorenz, S.: The role of subpolar deep water formation and Nordic Seas
600 overflows in simulated multidecadal variability of the Atlantic meridional overturning circulation.
601 *Ocean Sci.*, 10, 227-241, doi:10.5194/os-10-227-2014, 2014.

602 Lozier, M.S.: Deconstructing the Conveyor Belt, *Science*, 328, 1507-1511,
603 doi:10.1126/science.1189250, 2010.

604 Lozier, M.S., Roussenov, V., Reed, M.S.C., and Williams, R.G.: Opposing decadal changes for the
605 North Atlantic meridional overturning circulation. *Nature Geosci.*, 3, 728-734,
606 doi:10.1038/NGEO947, 2010.

607 Mahlstein I., and Knutti, R.: Ocean heat transport as a cause for model uncertainty in projected Arctic
608 warming, *J. Climate*, 24, 1451-1460, doi:10.1175/JCLI3713.1 ,2011.

609 Marsland, S.J., Haak, H., Jungclaus, J.H., Latif, M., and Roeske, F.: The Max- Planck- Institute global
610 ocean/sea-ice model with orthogonal curvilinear coordinates, *Ocean Modelling*, 5, 91-127, 2003.

611 Miettinen, A., Divine, D., Koç, N., Godtliobsen, F., and Hall, I.R.: Multicentennial variability of the sea
612 surface temperature gradient across the subpolar North Atlantic over the last 2.8kyr, *J. Climate*,
613 25, 4205-4219, doi:10.1175/JCLI-D-11-00581.1, 2012.

614 Mjell, T.L., Ninnemann, H.F., H.F. Kleiven, and Hall, I.R.: Multidecadal changes in Iceland-Scotland
615 overflow water vigori over the last 600 years and its relation to climate. Under review: *Geophys.*
616 *Res. Lett.*, 2014.

617 Müller, W.A., Matei, D., Bersch, M., Jungclaus, J.H., Haak, H., Lohmann, K., Compo, G.P.,
618 Sardeshmukh, P.D., and Marotzke, J.: A 20th century reanalysis-forced ocean model to reconstruct
619 the North Atlantic climate variations during the 1920s. *Clim. Dynam.*, in press: doi:
620 10.1007/s000382-014-2267-5, 2014.

621 Østerhus, S., and Gammelsrød, T.: The abyss of the Nordic Seas is warming. *J. Climate*, 12, 3297-3304,
622 1999.

623 Pavlov, A., Tverberg, V., Ivanov, B., Nilsen, F., Falk-Petersen, S., and Granskog, M.: Warming of
624 Atlantic Water in two west Spitsbergen fjords over the last century (1912-2009). *Polar Research*,
625 32, 11206, doi:10.3402/polar.v32i0.11206, 2013.

626 Polyakov, I.V., Alekseev, G.V., Timokhov, L.A., Bhatt, U.S., Colony, R.L., Simmons, H.L., Walsh, D.,
627 Walsh, J.E., Zakharov, V.F.: Variability of the Intermediate Atlantic Water of the Arctic Ocean over
628 the last 100 years, *J. Climate*, 17, 4485-4497, 2004.

629 Polyakov, I.V., Alexeev, V.A., Bhatt, U.S., Polyakova, E.I., and Zhang, X.: North Atlantic warming:
630 patterns of long-term trend and multidecadal variability. *Clim. Dynam.*, 34, 439-457,
631 doi:10.1007/s00382-008-0522-3, 2010.

632 Pongratz J., Reick, C.H., Raddatz, T., and Claussen, M.: A reconstruction of global agricultural areas
633 and land cover for the last millennium, *Glob. Biogeochem. Cycles*, 22, GB3018,
634 doi:10.1029/2007GB003153, 2008.

635 Rayner, N.A., Brohan, P., Parker, D.E., Folland, C.K., Kennedy, J.J., Vanicek, M., Ansell, T.J., and Tett,
636 S.F.B.: Improved analyses of changes and uncertainties in sea surface temperature measured in
637 situ since the mid nineteenth century: the HadSST2 data set. *J. Climate*, 19, 446-469,
638 doi:10.1175/jcli3637.1.

639 Reverdin, G.: North Atlantic Subpolar Gyre Surface Variability (1895-2009). *J. Climate*, 23, 4571-4584,
640 doi: 10.1175/2010JCLI3493.1, 2010.

641 Saenko, O.A., Fyfe, J.C., and England, M.H.: On the response of the oceanic wind-driven circulation to
642 atmospheric CO₂ increase. *Clim. Dynam.*, 25, 415-426, doi:10.1007/s00382-005-0032-5, 2005.

643 Schauer, U., Beszynnka-Möller, A., Walczowski, W., Fahrbach, E., Piechura, J., and Hansen, E.
644 Variations of measured heat flow through Fram Strait between 1997 and 2006, in: *Arctic-subarctic*
645 *ocean fluxes*, edited by Dickson, R.R., Meincke, J. and Rhines, P., Springer, Dordrecht, 65-85, 2008.

646 Schmidt, G.A., Jungclaus, J.H., Ammann, C.M., Bard, E., Braconnot, P., Crowley, T.J., Delaygue, G.,
647 Joos, F., Krivova, N.A., Muscheler, R., Otto-Bliesner, B.L., Pongratz, J., Shindell, D.T., Solanki, S.K.,
648 Steinhilber, F., Vieira, L.E.A.: Climate forcing reconstructions for use in PMIP simulations of the
649 last millennium (v.1.0), *Geosci. Model Dev.*, 4, 33-45, doi:10.5194/gmd-4-33-2011 ,2011.

650 Serreze, M.C., Barnett, A.P., Slater, A.G., Steele, M., Zhang, J., and Trenberth, K. E.: The large-scale
651 energy budget of the Arctic. *J. Geophys. Res.*, 112, D11122, doi:10.1029/2006JD008230, 2007.

652 Sedláček, J., and Mysak, L.A. A model study of the Little Ice Age and beyond: changes in ocean heat
653 content, hydrography and circulation since 1500. *Clim. Dynam*, 33, 461-475, doi: 10.1007/s00382-
654 008-0503-6, 2009.

655 Shaffrey, L., and Sutton, R.: Bjerknes compensation and the decadal variability of the energy
656 transports in a coupled climate model, *J. Climate*, 19, 1167-1448, doi:10.1175/JCLI3652.1, 2006.

657 Shi, F., Yang, B., Ljungqvist, F.C., and Yang, F.: Multi-proxy reconstruction of Arctic summer
658 temperatures over the past 1400 years, *Clim. Res.*, 54, 113-128, doi:10.3354/cr01112, 2012.

659 Skagseth, Ø., Furevik, T., Ingvaldsen, R., Loeng, H., Mork, K.A., Orvik, K.A., and Ozhigin, V.: Volume
660 and heat transport to the Arctic Ocean via the Norwegian and Barents Sea, in: *Arctic-subarctic*
661 *ocean fluxes*, edited by Dickson, R.R., Meincke, J., and Rhines, P., Springer, Dordrecht, 45-64,
662 2008.

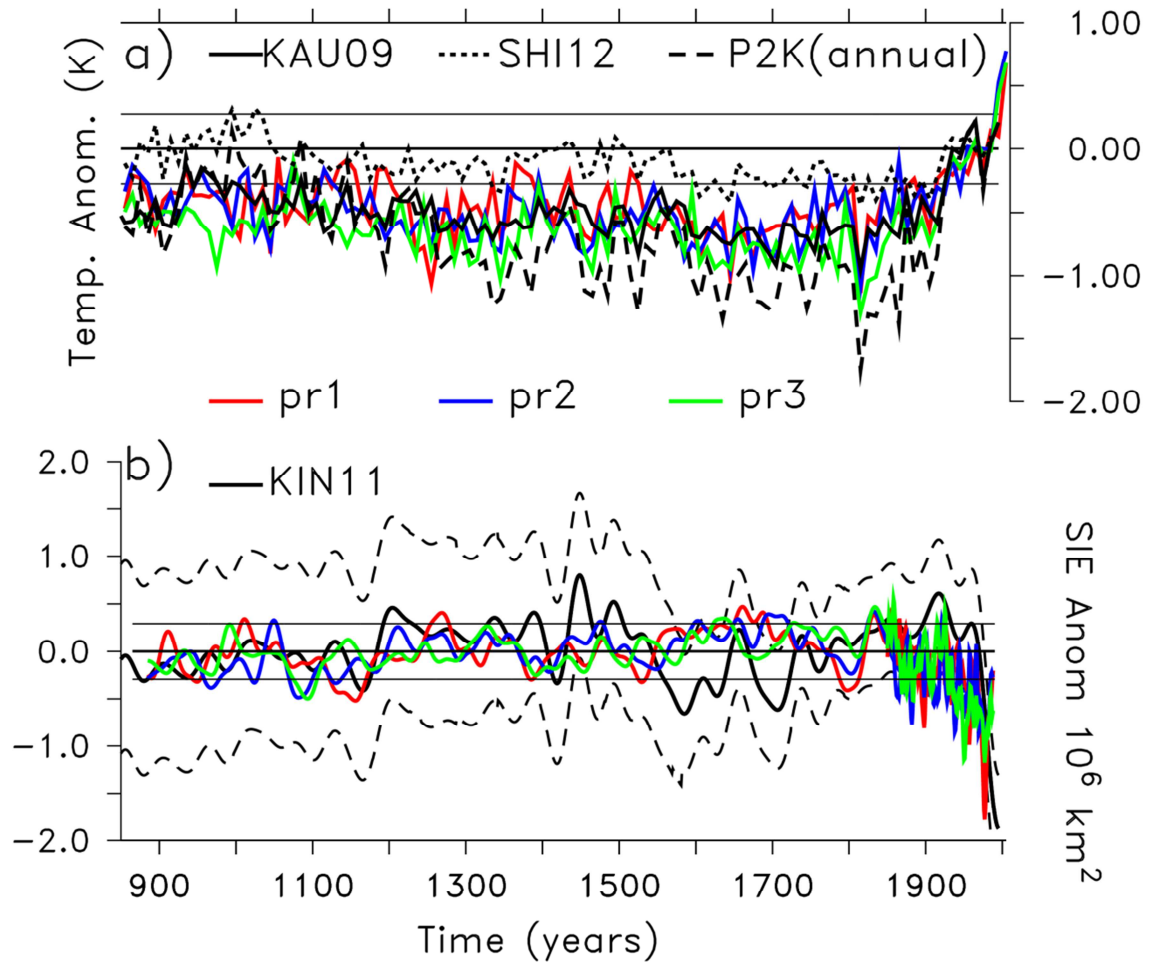
663 Smith, T.M., and Reynolds, R.W.: Improved extended reconstruction of SST (1854-1997). *J. Climate*,
664 17, 2466-2477, doi: 10.1175/1520-0442(2004)017<2466:IEROS>2.0.CO;2, 2004.

665 Spielhagen, R.F., Wagner, K., Sørensen, S.A., Zamelczyk, K., Kandiano, E., Budeus, G., Husum, K.,
666 Marchitto, T.M., and Hald, M.: Enhanced modern heat transfer to the Arctic by warm Atlantic
667 Water, *Science* 331 450-453, doi:10.1126/science.1197397, 2011.

668 Stevens, B., Giorgetta, M., Esch, M., Mauritsen, T., Crueger, T., Rast, S., Salzmann, M., Schmidt, H.,
669 Bader, J., Block, K., Brokopf, R., Fast, I., Kinne, S., Kornblueh, L., Lohmann, U., Pincus, R., Reichler,
670 T., and Roeckner, E.: Atmospheric component of the MPI-M Earth system Model: Echam6, *J.*
671 *Adv. Model Earth Syst.*, 5, 146-172, doi:10.1002/jame.20015, 2013.

672 Vieira, L.E.A., Solanki, S.K., Krivova, N.A., and Usoskin, I.: Evolution of the solar irradiance during the
673 Holocene, *Astron. Astroph.*, 531, A6, doi:10.1051/0004-6361/201015843, 2011.

- 674 Wang, Y.-M., Lean, J.L., Sheeley Jr., N.R.: Modeling the Sun's magnetic field and irradiance since
675 1713, *Astrophys. J.*, 625, 522-538, doi:10.1086/429689, 2005.
- 676 Werner, K., Spielhagen, R.F., Bauch, D., Hass, H.C., Kandiano, E., and Zamelcyk, K.: Atlantic water
677 advection to the eastern Fram Strait – multiproxy evidence for late Holocene variability,
678 *Paleogeography, Paleoclimatology, Paleoecology*, 308, 264-276, doi:10.1016/j.paleo.2011.05.030,
679 2011.
- 680 Zanchettin, D., Timmreck, C., Graf, H.-F., Rubino, A., Lorenz, S., Lohmann, K., Krüger, K., and
681 Jungclaus, J.H.: Bi-decadal variability excited in the coupled ocean-atmosphere system by strong
682 tropical volcanic eruptions, *Clim. Dynam.*, 39, 419-444, doi:10.1007/s00382-011-1167-1, 2012.
- 683 Zanchettin, D., Timmreck, C., Bothe, O., Lorenz, S.J., Hegerl, G., Graf, H.-F., Luterbacher, J., and
684 Jungclaus, J.H.: Background conditions influence the decadal climate response to strong volcanic
685 eruptions. *J. Geophys. Res. Atmos.*, 118, doi:10.1002/jgrd50229, 2013.
- 686 Zhang, R., Delworth, T.L., Sutton, R., Hodson, D.L.R., Dixon, K.W., Held, I.M., Kushnir, Y., Marshall, J.,
687 Ming, Y., Msadek, R., Robson, J., Rosati, A.J., Ting, M.F., and Vecchi, G.: Have aerosols caused the
688 observed Atlantic multidecadal variability? *J. Atm. Sci.*, 70, 1135-1144, doi:10.1175/JAS-D-12-
689 0331.11, 2013.
- 690

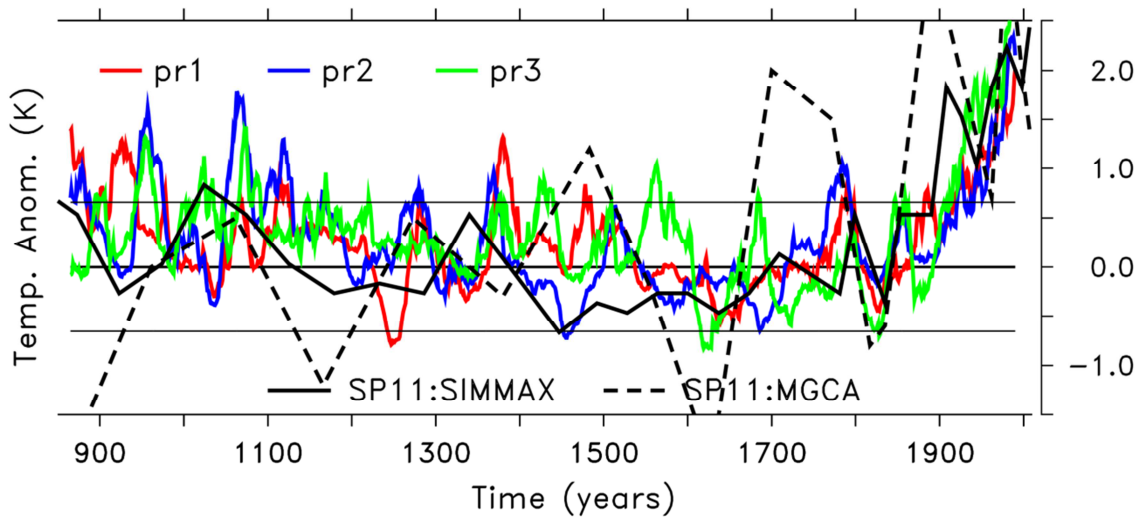


692

693

694 **Figure 1:** Simulated time series (colored lines for experiments pr1, pr2, pr3) of high northern latitude
 695 climate variables in comparison with reconstructions (black lines): **a)** 10-year averages of Arctic
 696 summer (JJA) surface air temperatures as anomalies w.r.t. the 1960-1990 mean. Summer
 697 temperature reconstructions are from: (solid black) Kaufman et al. (2009), and (dotted black) Shi et
 698 al. (2012). The PAGES2K reconstruction representing annual temperatures is also shown (dashed
 699 black). **b)** late-summer (August) sea-ice extent (in 10^6 km²) as anomalies w.r.t. the pre-industrial
 700 mean in comparison with the reconstruction by Kinnard et al. (2011): The thick black line denotes the
 701 40-year smoothed reconstruction, the dashed black lines their 95% confidence interval; for the
 702 simulations, a 41-yr running mean was applied for pre-industrial millennium and a 5-yr running mean
 703 for 1850-2005 to better display 20th century variability. Thin horizontal lines bracketing the zero line
 704 in **a)** and **b)** indicate the respective 2σ -ranges derived from the 1000yr-long PiCtrl experiment.

705

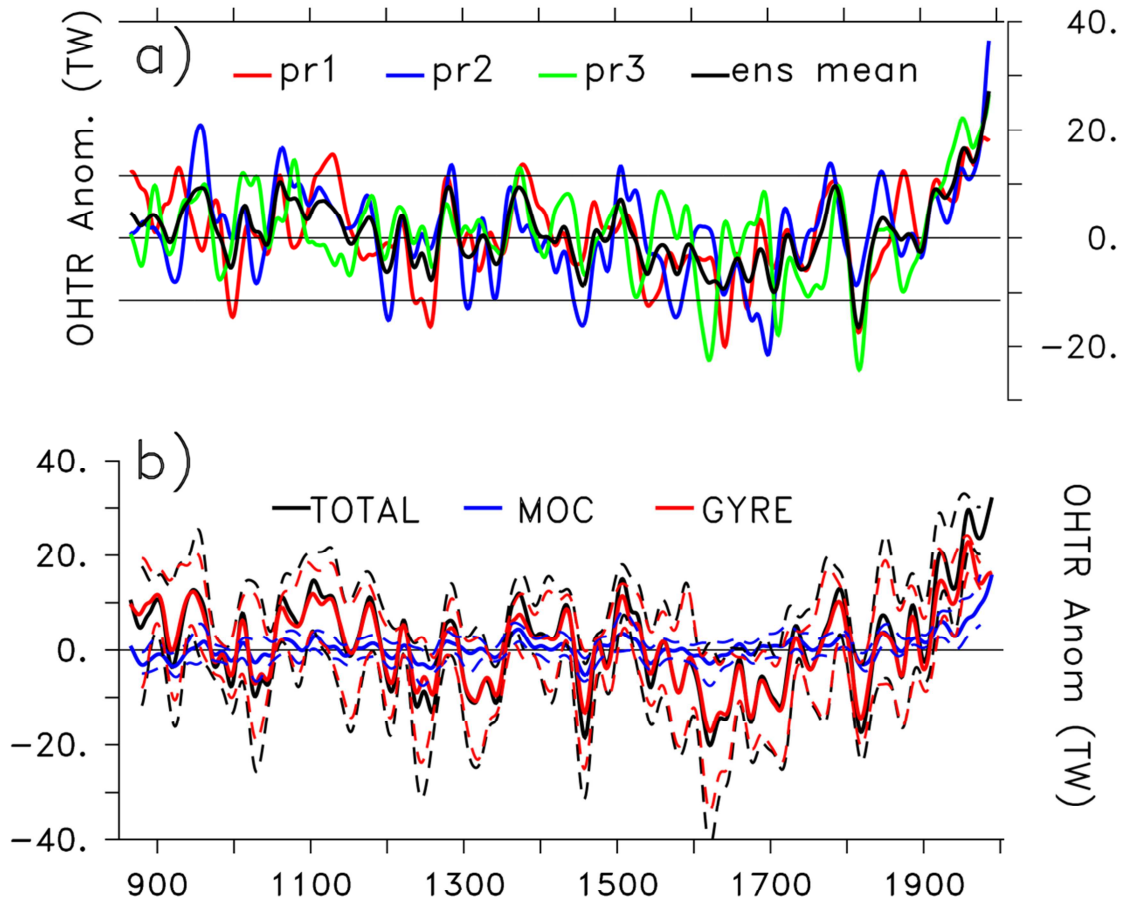


706

707 **Figure 2:** Simulated time series (colored lines for experiments pr1, pr2, pr3) of Atlantic Water
 708 temperature anomalies w.r.t. the pre-industrial mean in Fram Strait (78°N, 50m depth) in comparison
 709 with the reconstruction by Spielhagen et al. (2011) obtained by the (solid black) SIMMAX, and
 710 (dashed black) Mg/Ca methods, respectively. The thin horizontal lines bracketing the zero line
 711 indicate the respective 2σ -ranges derived from the 1000yr-long PiCtrl experiment.

712

713



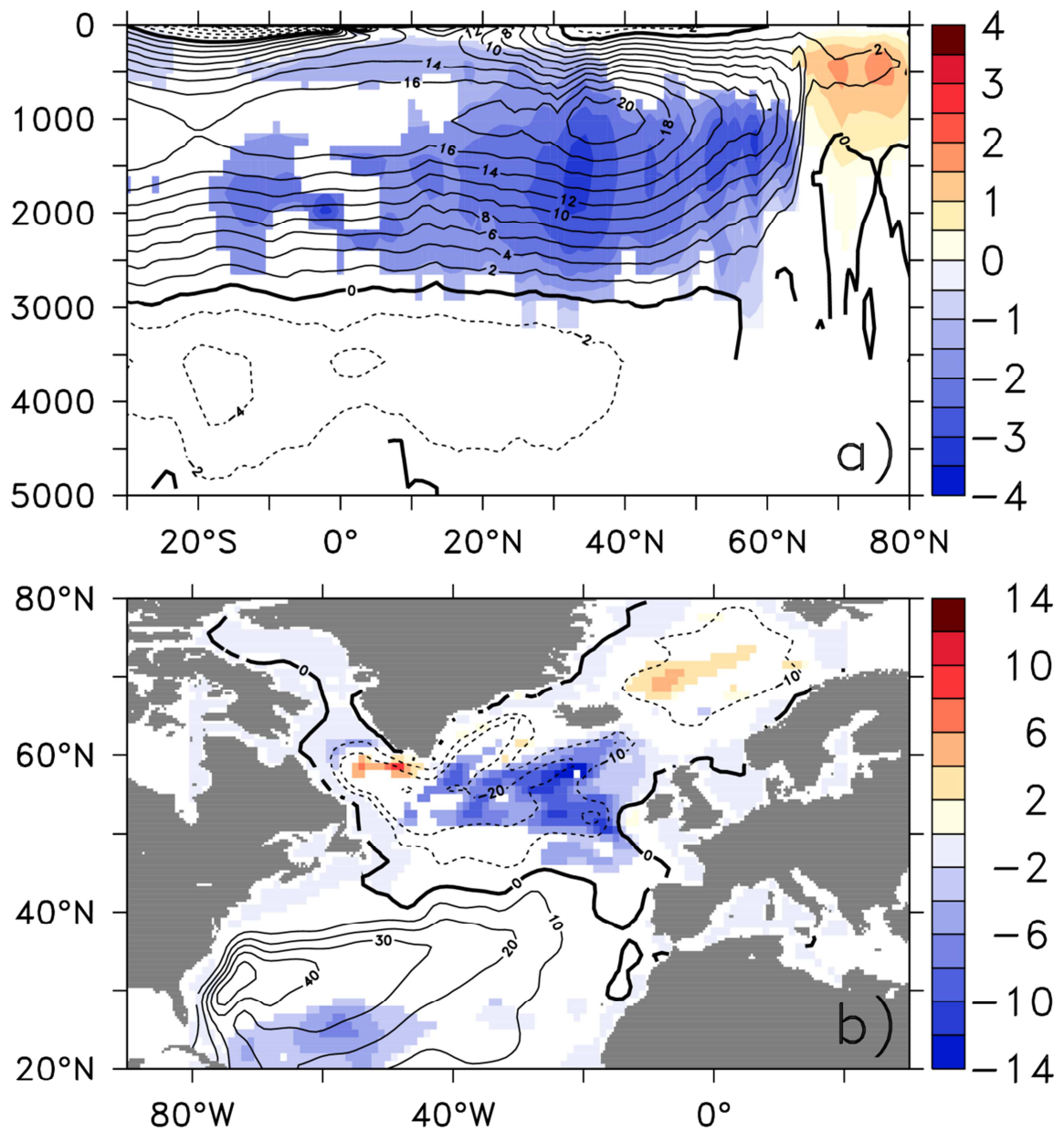
715

716 **Figure 3:** a) Simulated ocean heat transport (OHTR) to the Arctic (combined OHTR through Fram
717 Strait and Barents Sea Opening) as anomalies w.r.t. the pre-industrial mean; colored lines indicate
718 individual simulations pr1, pr2 and pr3, and the solid black line is the ensemble mean, thin horizontal
719 lines bracketing the zero line indicate the respective 2 σ -ranges derived from the 1000yr-long PiCtrl
720 experiment. b) Total OHTR (black lines, TOHTR) averaged over 60-65 $^{\circ}$ N, subdivided into gyre-related
721 OHTR (red, GOHTR), and overturning-circulation-related OHTR (blue, MOHTR). Thick lines represent
722 the ensemble means and the dashed lines the respective ensemble ranges. All time-series were
723 smoothed by a 31-yr running mean. Units are TW (1 TW = 10¹² Watt).

724

725

726



727

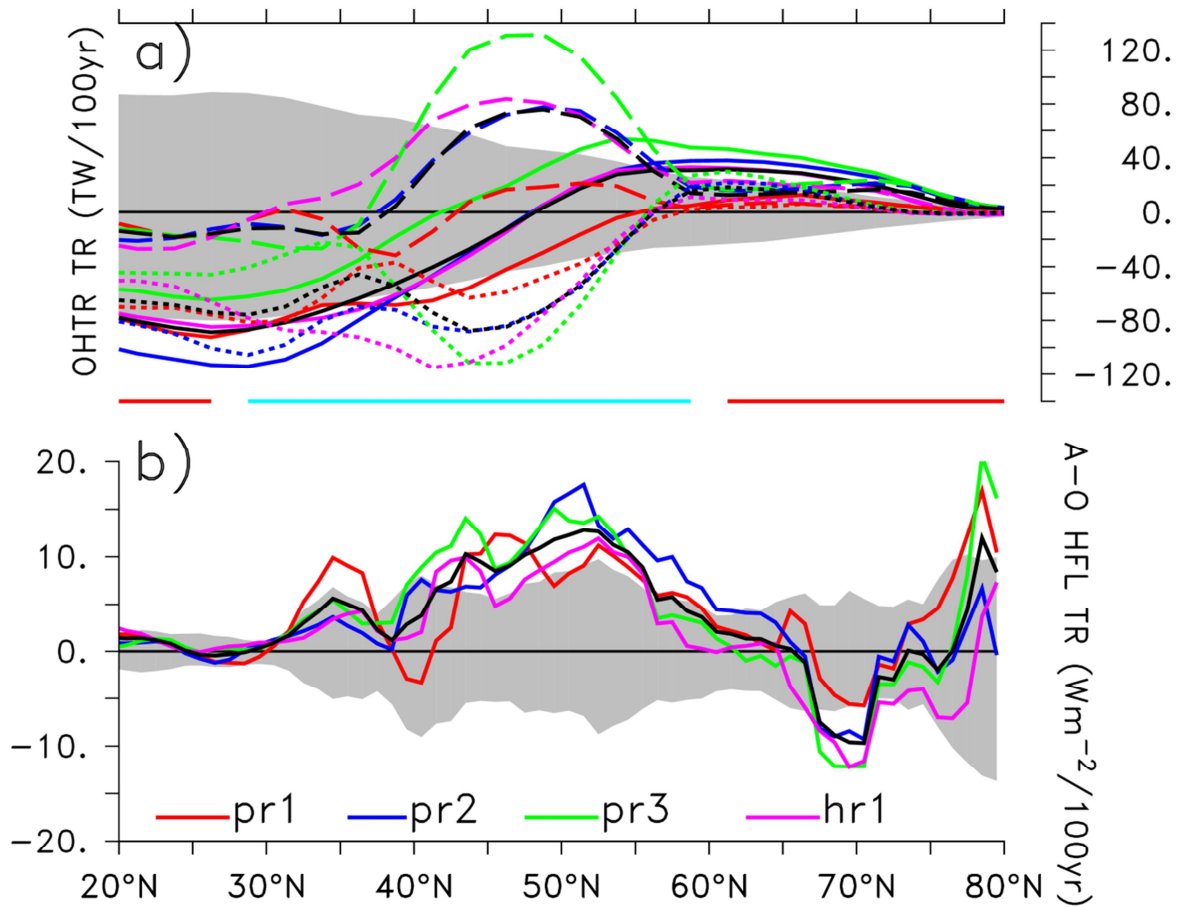
728

729 **Figure 4:** Simulated 20th century linear trends (1905-2005) in the pr2 simulation (color shading) of a)
 730 meridional overturning circulation, and b) barotropic stream function in the North Atlantic. Units are
 731 Sverdrups per 100 yrs ($1 \text{ Sv} = 10^6 \text{ m}^3 \text{ s}^{-1}$). Contour lines (contour intervals 2 Sv for overturning and 10
 732 Sv for barotropic stream function) describe the pre-industrial mean state. In both panels, only
 733 anomalies are shown that exceed the 5-95 percentile range of centennial trends derived from the
 734 PiCtrl simulations.

735

736

737



739

740

741 **Figure 5:** Simulated 20th century linear trends (1905-2005) as zonal averages over the Atlantic basin
 742 (experiments pr1, pr2, pr3, and hr1 as indicated by colored lines, black lines indicate ensemble
 743 means): **(a)** (solid lines) TOHTR, (dashed lines) GOHTR, and (dotted lines) MOHTR. Light-blue and red
 744 horizontal lines at the bottom of the plot indicate regions, where the ensemble-mean TOHTR
 745 divergence is positive (cooling by lateral advection: light-blue) or negative (warming by lateral
 746 advection: red). **(b)** atmosphere-ocean heat fluxes. Positive values indicate increased heat transfer
 747 from the atmosphere to the ocean or cooling of the atmosphere by the ocean. Colored lines are
 748 individual simulations and the black line is the ensemble mean. In **(a)** and **(b)**, the grey-shaded
 749 regions indicate the 5-95 percentile ranges of centennial trends in the unperturbed PiCtrl
 750 experiment.

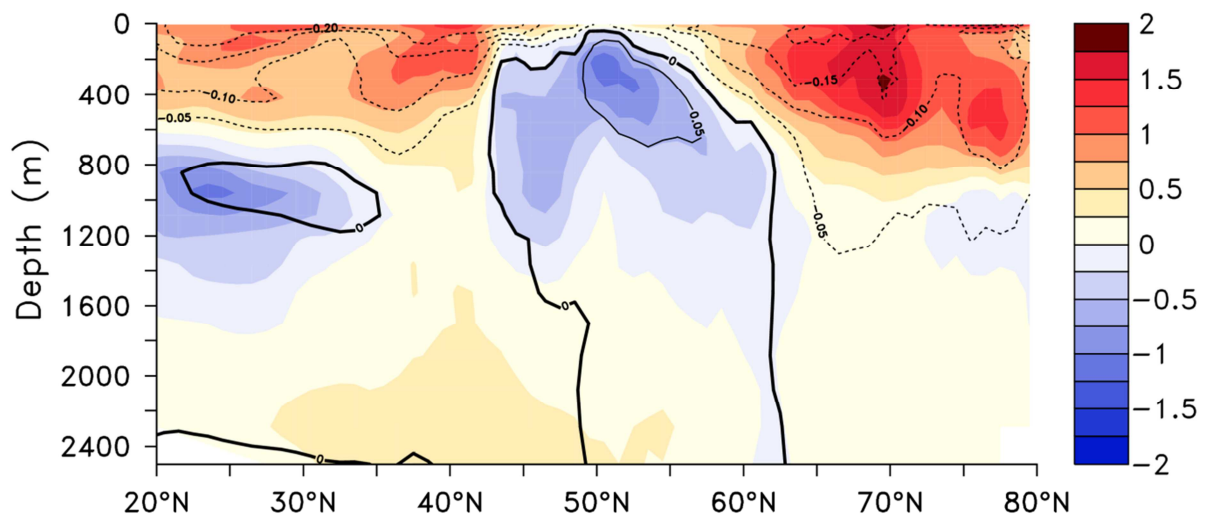
751

752

753

754

755



756

757

758 **Figure 6:** Simulated 20th century linear trends (1905-2005) as zonal averages over the Atlantic basin
759 for potential temperature (color shading) and density (contours, contour interval 0.05 kgm⁻³) trends
760 from the pr2 experiment.

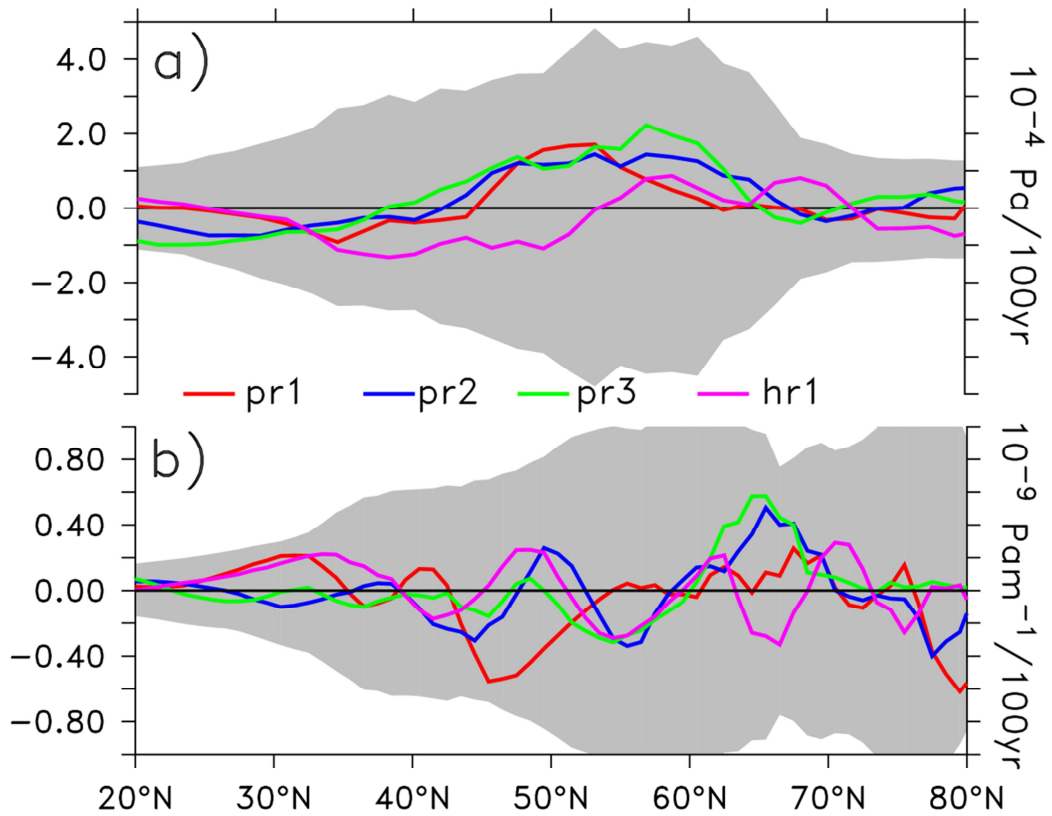
761

762

763

764

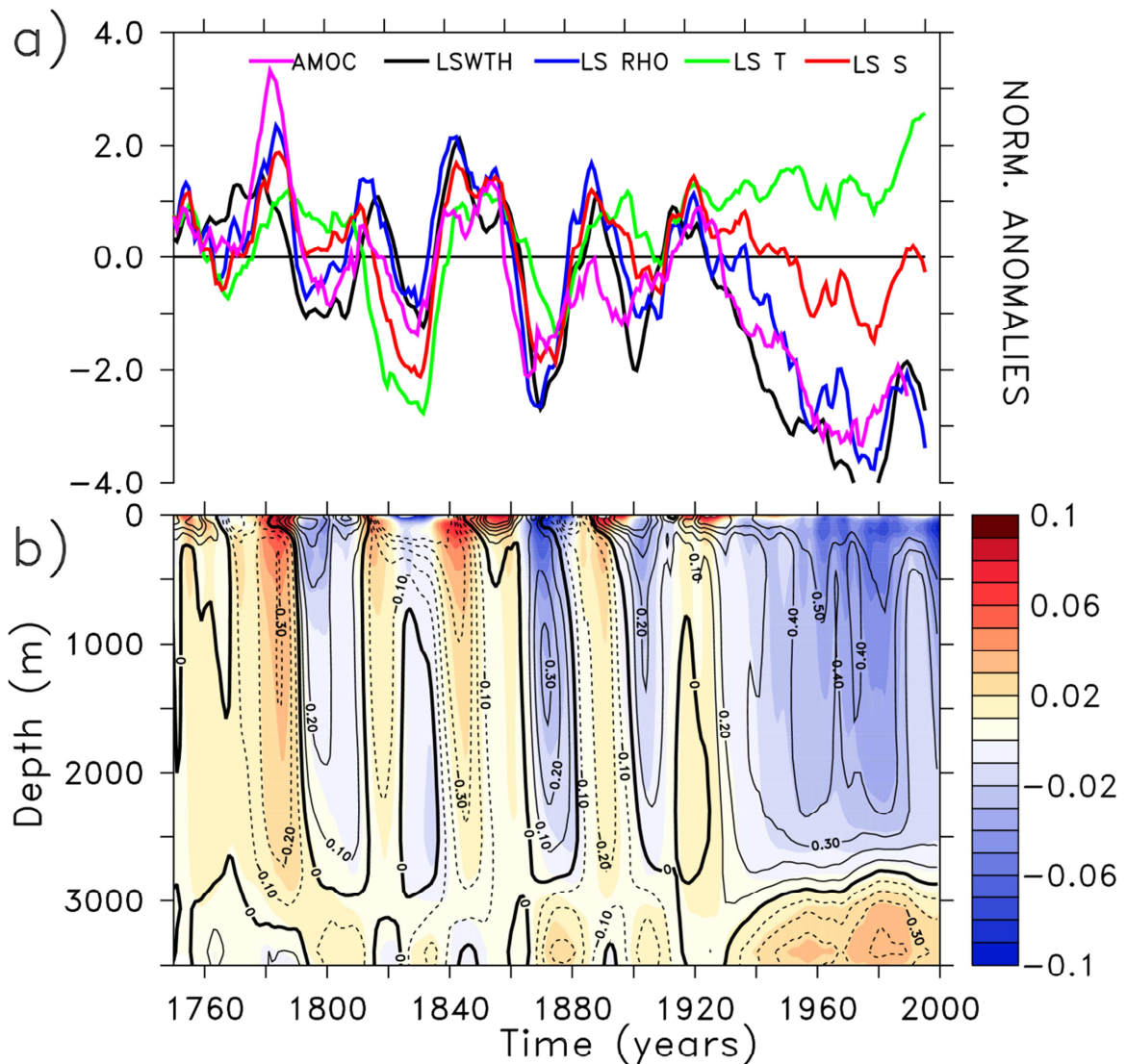
765
766
767



768
769

770 **Figure 7:** Simulated (experiments pr1, pr2, pr3, and hr1) 20th century linear trends (1905-2005) as
771 zonal averages over the Atlantic basin of **(a)** zonal wind stress (units 10^{-2} Pa/100 yrs) and **(b)**
772 wind stress curl (in 10^{-9} Pa m⁻¹/100yrs). Colored lines denote the experiments pr1, pr2, pr3, and hr1 and
773 the grey-shaded regions bracketing the zero line show the 5-95 percentile range of centennial trends
774 in the unperturbed PiCtrl experiment.
775

776
777

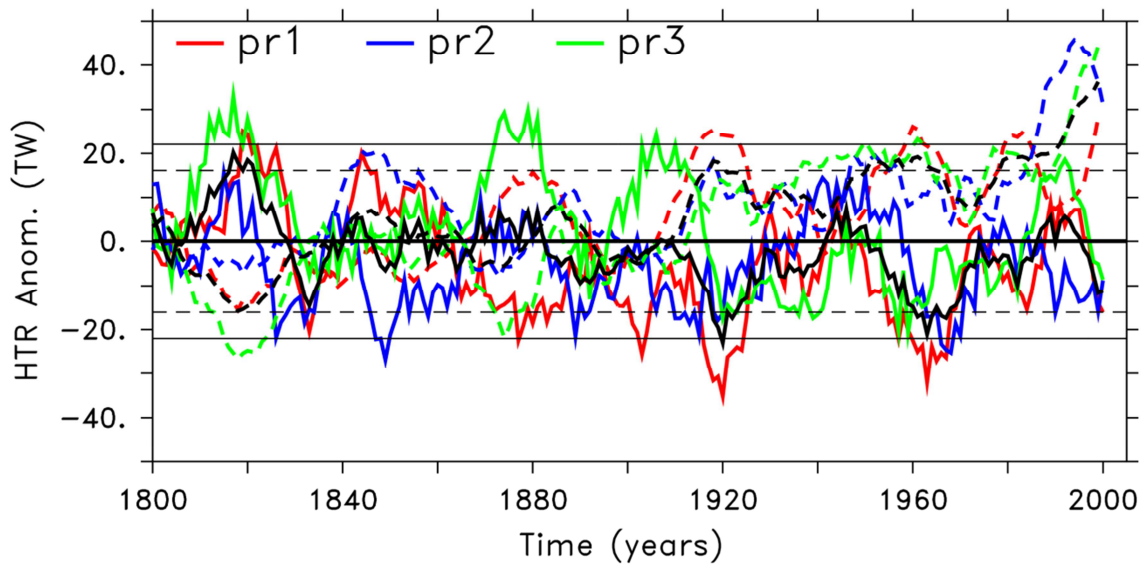


778

779 **Figure 8:** (a) Evolution of the Labrador Sea Water thickness (LSWTH, defined as the depth difference
 780 between the isopycnals $\sigma_2=36.74$ and $\sigma_2=36.82$, averaged over 60W-45W, 50N-60N), AMOC stream
 781 function at 30N and 1500m depth (displayed here with a 10-year time lag), and surface water mass
 782 properties in the region, where convection takes place in the Labrador Sea: Density (LS RHO),
 783 temperature (LS T), and salinity (LS S). All time-series are smoothed using an 11-yr running mean and
 784 are shown as normalized anomalies w.r.t. the pre-industrial means. (b) Evolution of potential density
 785 (color shading) and potential temperature (contours, contour intervals 0.05 K) as function of depth
 786 and time for the Labrador Sea in the pr2 simulation. An 11-yr running mean was applied to the data.

787

788



789

790 **Figure 9:** Time series of simulated (solid lines) atmospheric heat transports (AHTR) and (dashed lines)
 791 TOHTR at 70°N as anomalies w.r.t. the pre-industrial mean (colored lines for experiments pr1, pr2,
 792 pr3; time series shown as black dashed and solid lines denote the respective ensemble means).
 793 The horizontal black lines bracketing the zero lines are the respective 2- σ ranges derived from the
 794 PiCtrl experiment. An 11-yr running mean was applied to all data sets.

795